Structural and electronic phase transitions in $Zr_{1.03}Se_2$ at high pressure

Bishnupada Ghosh, Mrinmay Sahu, Debabrata Samanta, Pinku Saha,[*]
Anshuman Mondal,[†] and Goutam Dev Mukherjee[‡]

*National Centre for High Pressure Studies, Department of Physical Sciences, Indian Institute of Science Education
and Research Kolkata, Mohanpur 741246, Nadia, West Bengal, India*

We have carried out a detailed high pressure investigation using x-ray diffraction, Raman spectroscopy, and low temperature resistivity measurements on 1T $ZrSe_2$ having an excess of 3 at.% Zr. A careful x-ray diffraction data analysis shows that the sample undergoes a gradual structural transition to a monoclinic structure, with a mixed phase in the pressure range of 5.9 GPa to 14.8 GPa. We observe a minimum in the c/a ratio as well as in the full width at half maximum of the A_{1g} Raman mode at the same pressure in the parent 1T phase, which indicates an electronic phase transition. The sample shows a metallic characteristic in its low temperature resistivity data at ambient pressure, which persist until about 5.1 GPa and can be related to the presence of slight excess Zr. At and above 7.3 GPa, the sample shows a metal to semiconductor transition with the opening of a very small band gap, which increases with pressure. The low temperature resistivity data show an upturn, which flattens with the increase in pressure. The phenomenological analysis of the low temperature resistivity data indicates the presence of the Kondo effect in the sample, which may be due to the excess Zr.

I. INTRODUCTION

The growing importance of transition metal dichalcogenides (TMDs) in optoelectronic materials, data storage devices, sensors, spintronics, etc. has brought them to the focus of current research interest [1,2]. For understanding fundamental aspects of strong electron correlations, TMDs are ideal materials due to their diverse physical properties like strong spin orbit coupling, charge density wave, superconductivity, and Kondo effect [3–5]. TMDs stabilize in different structures and are associated with different stacking order. Most common polymorphs are trigonal (1T), hexagonal (2H), and rhombohedral (3R) phases (see [17], and references therein). The numbers inside the parentheses denote the number of layers in a unit cell. The hexagonal and the trigonal polymorphs are formed with different arrangement of chalcogen atom layers, where the 2H phase has trigonal prismatic coordination of metal atoms and the 1T phase has octahedral coordination of the metal atoms. Different morphologies lead to distinct electronic behavior, ranging from insulators, semiconductors, semimetal, and even superconductors [2,6–12]. Pressure is a very effective physical parameter which can tune the electronic behavior of TMDs by modifying their crystal structure in a controlled way [13–18]. Besides these, controlling layer numbers, presence of impurities, etc. can tune electronic properties of TMDs significantly [19–23].

Semiconducting TMDs from group IVB elements (Ti, Zr, and Hf) have not been studied as extensively as their counterparts from group VIB (Mo and W) [24]. $ZrSe_2$ and $HfSe_2$ semiconductors have band gap values similar to silicon ranging from 0.9 to 1.2 eV and can be a suitable replacement in the field of electronic devices [25]. During the fabrication of electronic devices, the TMDs are needed to be deposited on substrates, which may produce a large strain within the materials resulting in changes in the structural as well as electronic properties. Therefore, high pressure investigations of these materials are extremely important. A recent theoretical study has shown a pressure induced semiconductor to metal transition associated with a structural phase transition in ZrS_2 from the 1T phase ($P\bar{3}m1$ space group) at the ambient condition to the monoclinic phase at 2 GPa followed by the orthorhombic phase at 5.6 GPa [6]. A semiconductor to metallic transition is predicted for bilayer trigonal 1T-$ZrTe_2$ and hexagonal 2H-$ZrTe_2$ at pressures of 2 GPa and 6 GPa, respectively [17]. Also, other recent structural investigations in $MoTe_2$, WS_2, and $MoSe_2$ at high pressure have predicted electronic transitions driven by strain in the unit cell [13–16].

In this work we have carried out a detailed high pressure investigation on 1T $Zr_{1.03}Se_2$ using x-ray diffraction (XRD) and Raman spectroscopy measurements up to about 34.1 GPa. We have also performed temperature dependent resistivity [$\rho(T)$] measurements at selected pressure points up to about 8.1 GPa. From the XRD study a gradual structural phase transition from the 1T to the monoclinic phase is observed starting from 5.9 GPa, which completes at around 14.8 GPa. The Raman spectra also show noticeable changes above 5.9 GPa, which may be due to the change in symmetry associated with the structural transition. The temperature variation of resistivity of $Zr_{1.03}Se_2$ reveals a metallic character at ambient pressure due to the presence of excess Zr. At low temperatures, the $\rho(T)$

---

[*]Present address: Department of Earth Sciences, ETH Zürich, Zurich 8092, Switzerland.

[†]Present address: Institut für Mineralogie, University of Münster, Münster 48149, Germany.

[‡]Corresponding author: goutamdev@iiserkol.ac.in

shows an upturn indicating a possibility of the Kondo effect, resulting from the magnetic impurities associated to excess Zr. Above 5.1 GPa the increase in resistivity with the decrease of temperature shows a metal to semiconductor transition.

II. EXPERIMENTAL DETAILS

A high quality single crystal $ZrSe_2$ sample is purchased from HQ graphene (Netherlands) for carrying out the experiments. We have crushed a part of the sample and carried out powder XRD characterization procedure, which showed it to be in the 1T phase ($P\bar{3}m1$ space group), and will be discussed in detail in the next section. We have carried out EDAX measurements over a square area of about $10\,000\ \mu m^2$ of the sample using a 4×4 grid. We collected EDAX data from each part of the grid having an area of $625\ \mu m^2$. The 16 positions are shown in Supplemental Fig. S1 [26]. The stoichiometric ratios collected from the grids are given in Supplemental Figs. S2– S5 [26]. The average stoichiometric ratio of Zr and Se is found to be 1.03(1):2, indicating the presence of excess Zr in the sample.

XRD and Raman spectroscopy experiments at high pressures are carried out using piston-cylinder type diamond-anvil cell (DAC) from Almax easyLab. The diameter of the culets of the diamond anvils is $300\ \mu m$. A steel gasket is preindented to a thickness of $45\ \mu m$ by applying pressure using the DAC. A hole of $100\ \mu m$ diameter is drilled at the center of the preindented gasket. Small ruby chips (approximate size 3–$5\ \mu m$) are loaded along with the sample inside the hole to measure the pressure *in situ* during Raman spectroscopy experiments [27]. In the case of high pressure XRD measurements, a minute amount of silver powder is mixed with the sample, which acts as pressure calibrant for *in situ* high pressure measurements. A methanol-ethanol mixture in the ratio of 4:1 is used as a liquid pressure transmitting medium (PTM) in both cases to generate hydrostatic pressure. For Raman measurements, a Cobolt-samba diode pump laser of wavelength 532 nm is used for excitation. Laser power is kept constant to a maximum of 15 mW to avoid local heating of the sample. Raman spectra are collected in the backscattering geometry using a confocal micro-Raman system (Monovista from SI GmbH) consisting of a 750 mm monochromator and a back-illuminated PIXIS 100BR (1340×100) CCD camera. A $20\times$ infinitely corrected long working distance objective with numerical aperture 0.42 and laser spot diameter of about $5\ \mu m$ is used to collect the scattered light. The collection area on the sample is kept fixed throughout the whole experiment. The scattered light is dispersed using a grating with 1500 grooves/mm having a spectral resolution better than $1.2\ cm^{-1}$.

The x-ray source of XPRESS beamline in ELETTRA synchrotron with the wavelength of 0.4957 Å is used to perform high pressure XRD using the same diamond anvil cell configuration described above. The single crystal sample was crushed in an effort to obtain a powder and was used for the XRD study. The incident x-ray beam is collimated to $20\ \mu m$ diameter using a pinhole and passed through the center of the loaded gasket hole. A MAR 345 image plate detector system aligned normal to the beam is used to collect the diffracted XRD patterns. Sample to detector distance is calculated

using the XRD pattern of LaB_6. Acquired 2D XRD images are converted into intensity vs 2θ using DIOPTAS software [28]. Pressure is calibrated using third order Birch Murnaghan equation of state of silver [29]. X-ray diffraction patterns are indexed using CRYSFIRE software [30] followed by Rietveld refinements using GSAS software [31].

To investigate the pressure evolution of electronic behavior of 1T $Zr_{1.03}Se_2$ single crystal, low temperature and high pressure resistivity measurements are carried out in the ranges 22–300 K and 0–8.1 GPa, respectively. The low temperature and high pressure resistance measurements are performed using a miniature opposing plate type diamond anvil cell with diamonds having a culet diameter of $400\ \mu m$. A hole of $200\ \mu m$ diameter is drilled in the middle of a steel gasket preindented to a thickness of about $30\ \mu m$. A small amount of NaCl is put inside the hole as PTM and prepressed inside the hole. Next a dried mixture of alumina powder and epoxy (approximately 4:1 mass ratio) is spread on the gasket and pressed using two diamond culets by applying pressure up to about 10 GPa. This helps to insulate the gasket and the electrical probes. A square shaped sample is cut and kept in the middle of the insulated gasket hole. Four thin gold wires prepressed and placed on the sample surface are used as four probes for resistance measurements using the van der Pauw method, which is well accepted in the resistivity measurements using a DAC [32,33]. The loaded DAC is placed inside a closed cycle cryostat for low temperature high pressure measurements. Keithley current source (Model No. 6221) and nanovoltmeter (Model No. 2182A) are used to source the current and measure the voltage, respectively. The schematic diagram of the loaded diamond anvil cell is shown in Supplemental Fig. S6 [26]. Pressure is measured using the ruby fluorescence technique. To check the existence of insulation between the gasket and the sample, we carry out a periodic check during the experiments. Measurements are performed by changing the leads alternately and taking the average value of resistivity. In the first configuration current is sourced through first and second leads and voltage is measured across third and fourth leads, and in the second configuration current is sourced through second and third leads and voltage is measured across first and fourth leads to overcome pressure inhomogeneity. The resistivity of the sample is calculated using the simple formula [13,34]

$$\rho = R\frac{A}{l},\tag{1}$$

where ρ and R are the resistivity and the resistance of the sample, respectively, l is the distance between two electrodes, and A represents the product of sample thickness and the lateral width of the sample. The pressure exerted on the sample is pseudohydrostatic. We have used an almost square shaped sample, by exfoliating from a single crystal. Since it was not possible to determine the actual change in thickness of the sample with pressure, we assumed it to be constant.

III. RESULTS AND DISCUSSION

A. X-ray diffraction studies

The ambient XRD pattern of $Zr_{1.03}Se_2$ is indexed to the 1T crystal structure in $P\bar{3}m1$ space group symmetry with lattice
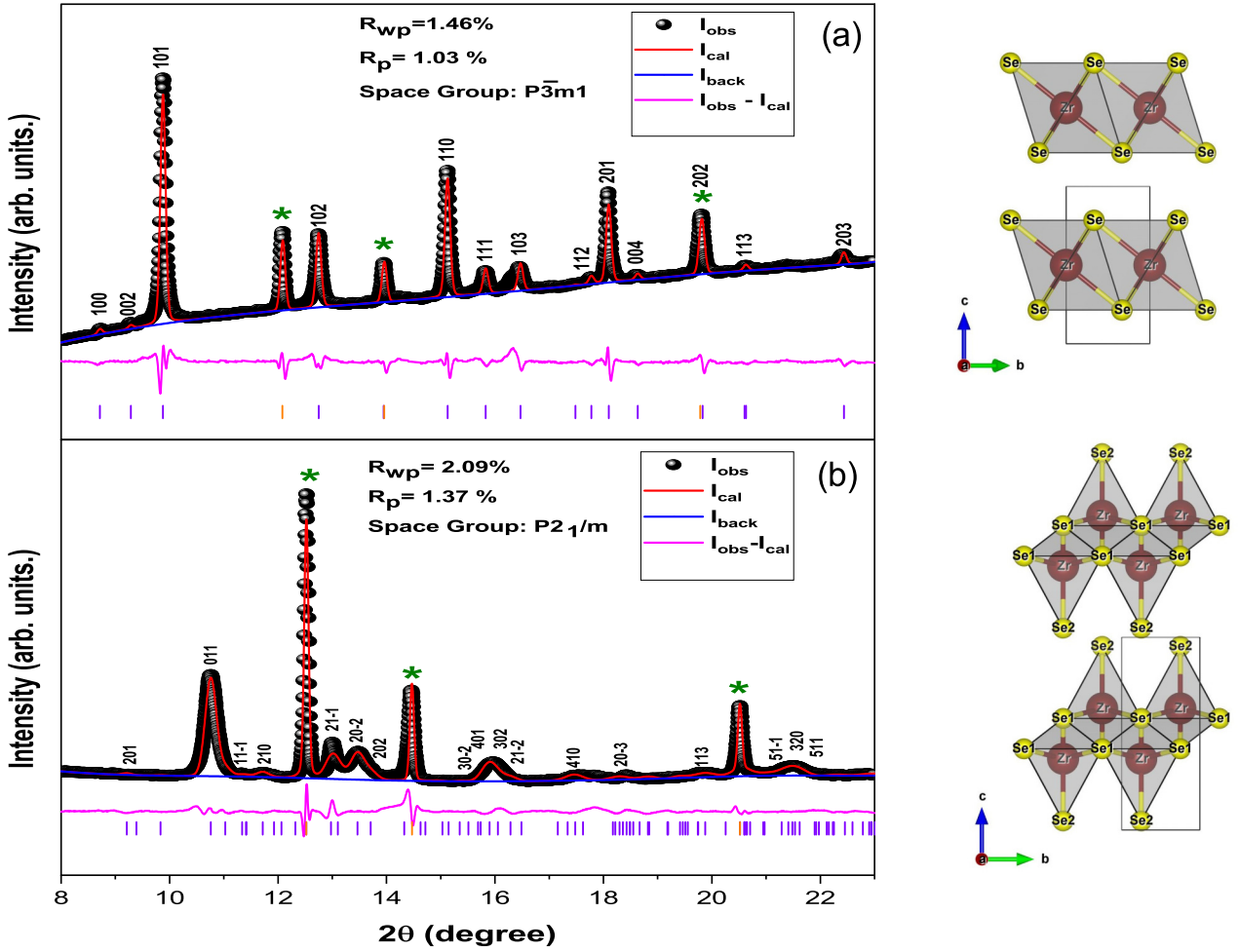
FIG. 1. Rietveld refinements of (a) XRD pattern at ambient pressure in the 1T phase and (b) XRD pattern at 14.8 GPa pressure in the monoclinic phase. Atomic orientations inside the unit cell of $Zr_{1.03}Se_2$ crystal in 1T as well as the monoclinic phase are shown in the right side of the graphs. Silver peaks are marked by green star.

parameters $a = 3.7661(3)$ Å, $c = 6.1239(10)$ Å and unit cell volume $V = 75.22(2)$ Å^3 and $Z = 1$, which matches well with the literature [24]. Rietveld refinement of the ambient XRD pattern is carried out using the atom positions given by Zhai *et al.* [6] as the starting model. Figure 1(a) shows the Rietveld refinement of the XRD pattern of $Zr_{1.03}Se_2$ at ambient pressure. The atomic arrangements inside a unit cell are shown in Fig. 1(a). The refined atom positions are given in Table I. In a layer of $Zr_{1.03}Se_2$, Zr atoms are sandwiched between Se atoms as shown in Fig. 1(a).

In Fig. 2, we have presented the pressure evolution of XRD patterns at selected pressure points up to 30.9 GPa

(XRD patterns at lower pressure regions are shown in Supplemental Fig. S7 [26]). The XRD Bragg peaks corresponding to the Ag pressure marker are indicated by star. All XRD Bragg peaks broaden with pressure and shift towards higher 2θ values due to unit cell volume compression. Around 5.9 GPa certain new peaks around $2\theta = 10.52°$, $12.47°$, $12.85°$, $17.68°$, and $21.10°$ (shown in Fig. 2 using arrow) appear. The new XRD pattern could not be indexed to the parent 1T phase. Above 5.9 GPa, the intensity of (101) Bragg peak of the parent 1T phase reduces continuously and disappears around 14.8 GPa. The intensities of the new peaks, those appearing around 5.9 GPa, grow with pressure. This indicates

TABLE I. Structural parameters of different phases.

Phase	Lattice parameters (Å)	Atoms	x/a	y/b	z/c	Pressure (GPa)
$P\bar{3}m1$	$a = b = 3.7661(3)$	Zr1(1b)	0(0)	0(0)	0.5000(0)	0.0
	$c = 6.1239(10)$	Se1(2d)	0.6667(0)	0.3333(0)	0.7852(3)	
$P2_1/m$	$a = 4.9785(13)$	Zr1(2e)	0.6686(4)	0.2500(0)	0.3694(8)	14.8
	$b = 3.1199(4)$	Se1(2e)	0.8470(2)	0.2500(0)	0.5788(2)	
	$c = 7.7119(20)$	Se2(2e)	0.8220(3)	0.2500(0)	0.0473(2)	
	$\beta = 91.10(2)°$					
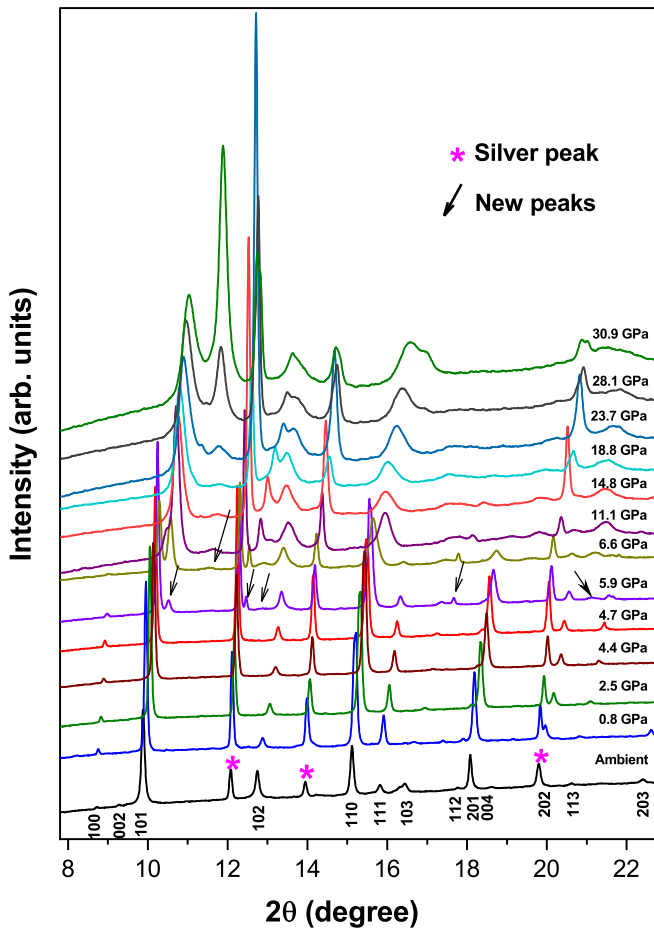
FIG. 2. Pressure evolution of XRD patterns. Ag peaks are shown with pink star. New Bragg peaks appearing around 5.9 GPa are denoted by arrows.

a gradual growth of a new structural phase with pressure, in parallel with the continuous disappearance of the parent 1T phase, indicating a mixed phase in the pressure range of 5.9 to 14.8 GPa. The XRD pattern at 14.8 GPa is indexed to a monoclinic structure with a high figure of merit having lattice parameters $a = 4.9785(13)$ Å, $b = 3.1199(4)$ Å, and $c = 7.7119(20)$ Å, monoclinic angle $\beta = 91.10(2)°$, and unit cell volume $V = 119.76(3)$ Å^3 with $Z = 2$. Analyzing our d values using CHEKCELL [35] returned a best space group $P2_1/m$. A similar study by Martino *et al.* [36] shows a new orthorhombic phase of ZrSe$_2$ to appear along with the parent 1T phase around 8 GPa. They found coexistence of 1T and orthorhombic phases up to 11.5 GPa, the highest pressure in their study. We also could index the XRD pattern to an orthorhombic phase in space group *Immm*, similar to that predicted by Martino *et al.* [36]. However, profile fitting followed by the Rietveld refinement using the orthorhombic structure did not result in a good fit (Supplemental Fig. S8 [26]). Therefore, we proceed with the Rietveld refinement of the high pressure phase using the obtained lattice parameters in the monoclinic crystal structure. We used the atom positions of the similar high pressure monoclinic phase of the sister material ZrS$_2$ as reported by Zhai *et al.* [6]. In Fig. 1(b), we have shown the Rietveld refined pattern of our monoclinic

phase, which shows an excellent fit. A comparison of the Rietveld refinements between both high pressure structures is shown in the Supplemental Material in Fig. S8 and Fig. S9 [26]. However, we would like to mention that the Bragg peaks (3 0 −2), (4 0 1), (3 0 2), and (2 1 −2) are slightly affected due to specific orientation at high pressure. In Table I we have given the new atom positions for the monoclinic phase and the unit cell structure is shown in Fig. 1(b). The new monoclinic unit cell consists of distorted ZrSe$_6$ octahedra arranged in a layer. It will be worthwhile to discuss the main differences between our work and the high pressure XRD study of Martino *et al.* [36], which lies mainly in the experimental methodology. The latter study used a laboratory x-ray source for high pressure XRD measurements. The laboratory x-ray sources have much lesser photon flux and broad beam size compared to synchrotron sources as seen from background contributions from the steel gasket, even though they have a gasket hole size of about 250 μm. Therefore, the XRD patterns obtained by them suffer from broader as well as low intensity Bragg peaks at high pressures. In contrast, our high pressure XRD studies are carried out in a synchrotron with a very high photon flux, small beam size (about 20 microns), and lower wavelength. These improved experimental parameters allow us to study the sample in more detail and with better accuracy.

The XRD pattern in the pressure range 5.9–12.1 GPa now could be fitted using the mixed phase of the parent 1T and the new monoclinic phase. With increasing pressure, the fraction of the parent 1T phase decreases and the new monoclinic phase increases with a complete transformation above 12.1 GPa. The variation of phase fraction ratio obtained from the Rietveld refinements is shown in the Supplemental Fig. S10 [26]. Rietveld refinement of XRD pattern using the mixed phase at 10.4 GPa is shown in Supplemental Fig. S11 [26]. The variation of the relative lattice parameters of the 1T phase is shown in Fig. 3(a). We find that the a axis is compressed almost linearly with pressure, whereas the c axis reduces rapidly up to about 5.9 GPa with compression of about 5.7%, and then it almost saturates in the mixed phase. To understand the anomalous compression behavior of the 1T unit cell, we have plotted the c/a ratio in Fig. 3(b), which shows a sharp minimum at about 5.9 GPa. The c/a ratio is associated with the lattice strain in any hexagonal structure. Decreasing c/a ratio indicates a decrease in the internal strain of the unit cell until the phase transition to the mixed phase. In layered materials, due to van der Waals interaction among the layers along the c axis, the initial increase in pressure is generally found to compress the c axis significantly in comparison to the ab plane. However, above 5.9 GPa, in the compact structure, the c axis cannot be compressed anymore significantly, resulting in an increase in the lattice strain in the ab plane. It may be suggested that the anisotropic compression of the parent 1T phase leads to such a structural transition, which results in an increase in the lattice strain in the compressed unit cell of the parent structure. The pressure evolution of relative lattice parameters of the monoclinic phase from 5.9 GPa to 30.9 GPa is shown in Fig. 3(c). The b and c axes are found to reduce almost linearly with pressure for the whole pressure region. The a axis decreases with pressure up to 12.1 GPa; then it starts to increase at higher pressures. The monoclinic angle β also shows a similar variation. It decreases
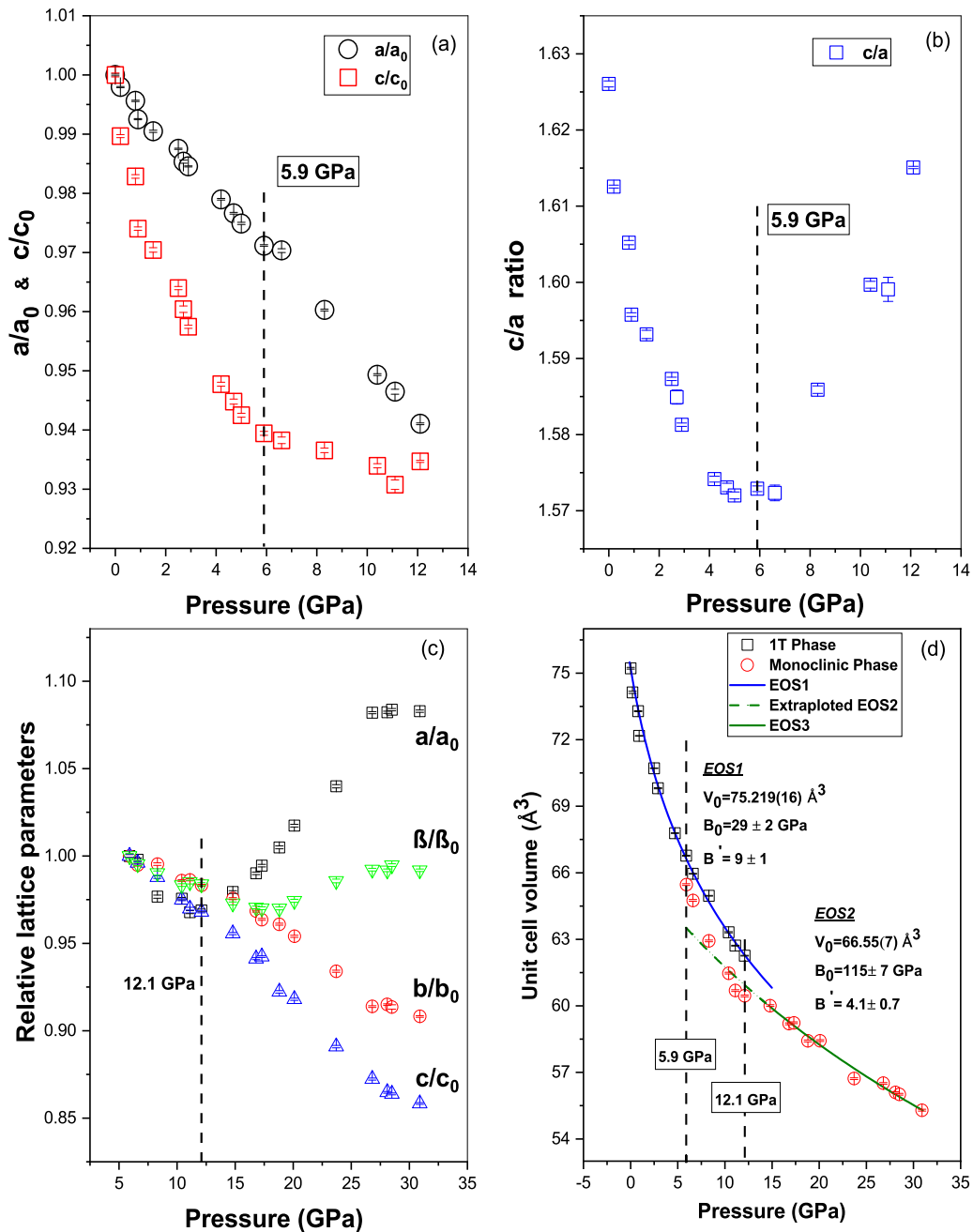
FIG. 3. Pressure evolution of (a) the relative lattice parameter of 1T phase, (b) c/a ratio of 1T phase, and (c) relative lattice parameters of monoclinic phase. (d) The variation of unit cell volume with applied pressure for two phases. The lines through data points show the EOS fits.

with pressure at first but then starts to increase above 17 GPa. At the highest pressure of this experiment the a axis increases by 8.34%, whereas b and c axes decrease by 9.3% and 14.16% of their initial values, respectively. The c axis is the most compressible axis. The pressure evolution of relative lattice parameters shows an anisotropic compression along different directions resulting in differential strain inside the sample. At higher pressures, where b and c axes experience compressive strain, tensile strain develops along the a axis.

The variation of unit cell volume with applied pressure for both the phases is shown in Fig. 3(d). The unit cell volume vs pressure data for 1T phase is fitted using single third order BM EOS [37,38]. The EOS fit is carried out by using the

ambient volume as obtained from the Rietveld refinement of the ambient XRD pattern and keeping it constant. The bulk modulus B_0 and its first pressure derivative B' for the 1T phase are found to be 29(2) GPa and 9(1), respectively, indicating a large pressure dependent compressibility. The unit cell volume of the monoclinic phase shows a slope change at the boundary of the mixed phase and the pure monoclinic phase of the sample with a possibility of an isostructural transition. We have not carried out any EOS fitting in the small pressure range of 5.9 to 14.8 GPa due to a lower number of data points. Pressure vs unit cell volume of a monoclinic cell above 14.8 GPa is fitted using a third order BM EOS. This gives a value of $V_0 = 133.1(7)$ Å^3 and $B_0 = 115(7)$ GPa

and $B' = 4.1(7)$. Extending the high pressure EOS fit of the monoclinic phase down to about 5.9 GPa [dotted green line in Fig. 3(d)] shows that it represents well the pressure behavior of volume up to about 10 GPa. The monoclinic phase volume seems to be more compressible in the range of 5.9 to 10 GPa in comparison to that above 10 GPa. Since the liquid PTM freezes above 10 GPa, the effect of nonhydrostatic stress resulting in a differential strain on the layered material cannot be ruled out. The B_0 for the monoclinic phase is found to be four times larger than the 1T phase. However, for a better comparison, we have calculated the pressure dependent bulk modulus B_P at a few pressures in the mixed phase range [26]. For the 1T phase the B_P values at about 10.4, 11.1, and 12.1 GPa are calculated to be 100(2), 105(2), and 110(3) GPa, respectively. At the same pressures, for the monoclinic phase, the B_P values are calculated to be 156(7), 164(8), and 167(8) GPa, respectively. It can be seen that the compressibility of the monoclinic phase remains lower in comparison to the 1T phase and the compressibility decreases further with the increase in pressure.

B. Raman spectroscopy studies

The ambient Raman spectrum is shown in Fig. 4(a). We observe an intense mode at 195 cm^{-1} and a mode with lower intensity at 147 cm^{-1}. In addition, we observe a very low intense peak at 109 cm^{-1} and a broad hump in the region from 235 cm^{-1} to 280 cm^{-1}. The humplike feature can be fitted into two Raman modes at around 239 cm^{-1} and 267 cm^{-1} as shown in the inset of Fig. 4(a). The spectrum is found to be similar to that reported by Manas-Valero *et al.* [24]. Following the literature, we have indexed the Raman modes as follows: (i) 195 cm^{-1} as A_{1g}, (ii) 147 cm^{-1} as E_g, and (iii) 109 cm^{-1}, 239 cm^{-1}, and 267 cm^{-1} as two phonon modes. A_{1g} mode is due to the out of plane vibration of Se atoms against each other and E_g mode is due to the in-plane vibrations of Se atoms against each other [24,39]. In Fig. 4(b) pressure evolution of Raman spectra at selected pressure points is shown up to 34.1 GPa (pressure evolution of all Raman spectra is shown in Supplemental Fig. S12 [26]). The mode frequency of A_{1g} mode shifts towards higher wave number with pressure and its intensity decreases with increasing pressure. At 5.9 GPa, changes in the shape of the Raman spectrum are observed in the form of the appearance of broad humps around the parent E_g and A_{1g} modes. These broad humps give rise to well defined peaks above 7.2 GPa. These new peaks are labeled as P1, P2, P3, P4, and P5 at around 108, 127, 166, 245, and 272 cm^{-1}, respectively, and are marked in Fig. 4(b) at 7.9 GPa. The appearance of new Raman modes can be attributed to the change in symmetry in the crystal around 5.9 GPa due to the appearance of a new monoclinic crystal structure along with the parent 1T crystal structure. The XRD results show a mixed phase in between 5.9 and 12.1 GPa. Possibly, the Raman modes due to both the phases overlap and show a broad feature in the Raman spectra as seen at 5.9 GPa and 6.5 GPa [Fig. 4(b)]. The pressure evolution of Raman shift for all the detected modes is shown in Fig. 5(a). The pressure variation of A_{1g} mode frequency could be fitted linearly with a slope of 3.61 cm^{-1} GPa^{-1} up to 6.5 GPa, which then almost saturates above 7.2 GPa. Even though the
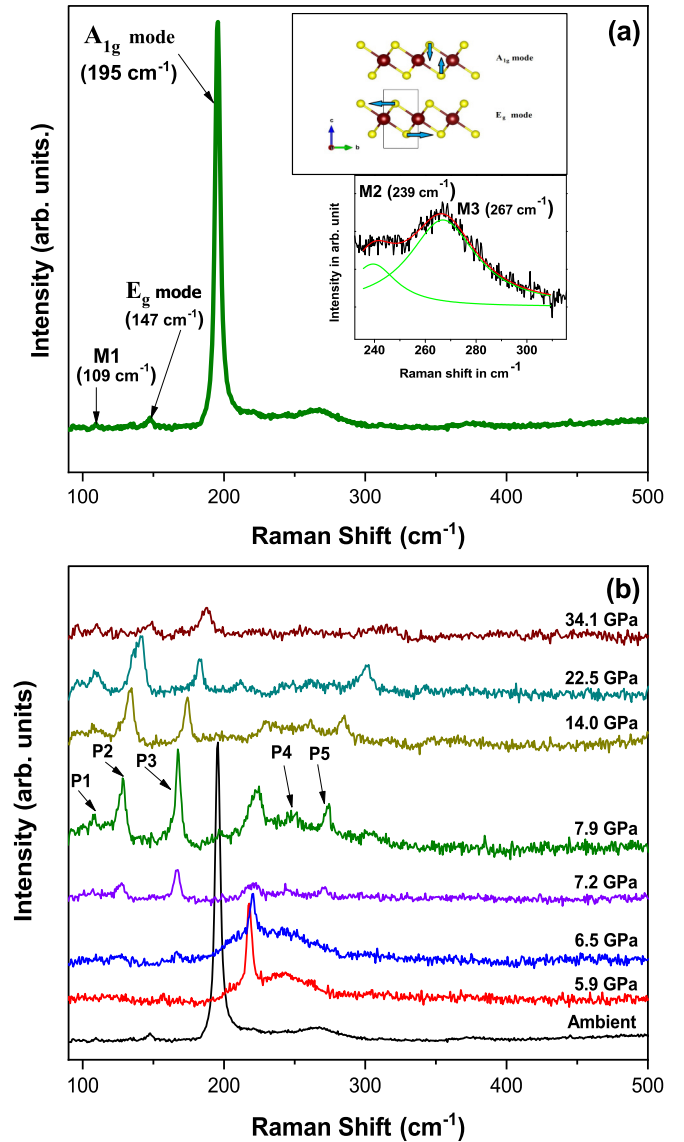
FIG. 4. (a) Ambient Raman spectrum of $Zr_{1.03}Se_2$ using 532 nm laser as excitation source. E_g and A_{1g} mode vibrations are shown in the inset. Two phonon modes around 239 cm^{-1} and 267 cm^{-1} are also shown in the inset of the figure. (b) Pressure evolution of Raman spectra at selected pressure points. P1, P2, P3, P4, and P5 denote the new Raman modes in the monoclinic phase.

compressibility in the monoclinic phase is lower compared to the 1T phase, it cannot justify the sudden saturation effect of the A_{1g} mode alone, since all other modes show a reasonable pressure effect. The change in FWHM with pressure for the A_{1g} mode is shown in Fig. 5(b). FWHM of the A_{1g} mode shows a minimum around 5 GPa [shown in the inset of Fig. 5(b)] and then suddenly jumps above 6.5 GPa pressure. A decrease in the Raman mode bandwidth is associated with an increase in phonon lifetime due to a decrease in anharmonic scattering. The minimum in the FWHM of the Raman mode is generally associated with an electronic transition in these layered materials [14,15]. It may be noted here that the c/a ratio also shows a minimum at the same pressure. The hydrostatic limit of the methanol-ethanol PTM is 10 GPa [40], which is much
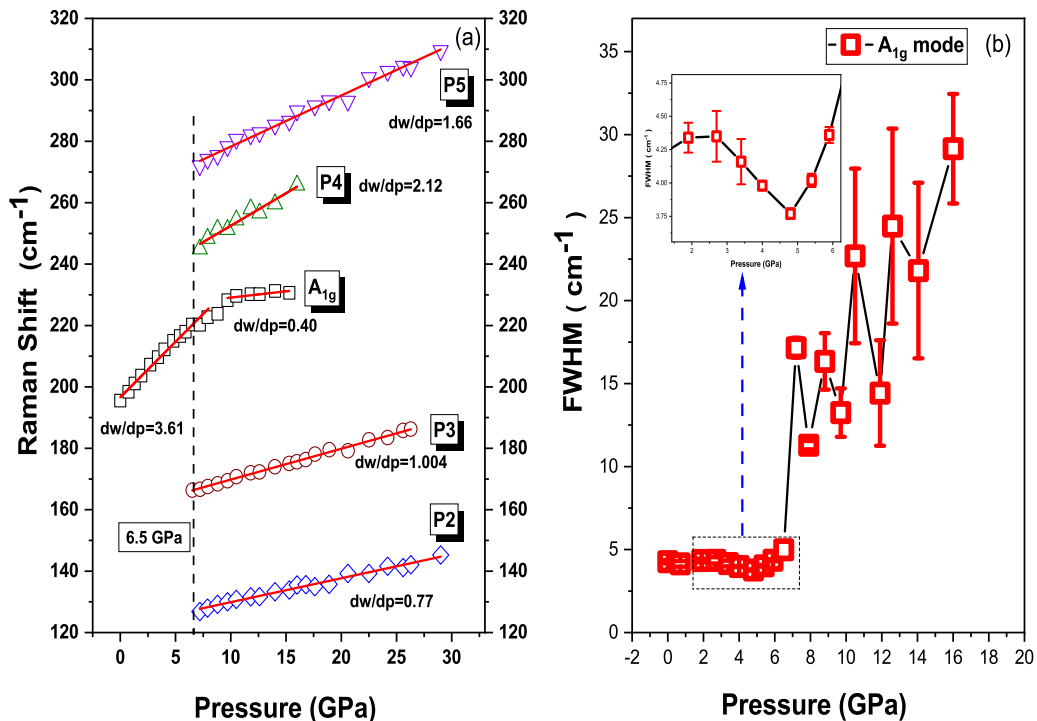
FIG. 5. (a) Pressure variation of Raman mode frequencies. (b) Pressure variation of FWHM of the A_{1g} Raman mode, with the inset showing the zoomed part marked by the box.

higher than the pressure where FWHM of the A_{1g} mode starts to increase rapidly, indicating the observed effect is due to pressure induced changes in the sample physical properties. The sudden jump above 6.5 GPa can be associated with the increased anharmonic phonon-phonon interactions due to the structural transition along with the increase in lattice strain.

C. Pressure and temperature dependence of electrical resistivity

In order to study the electronic behavior of this material under pressure, we have carried out resistivity (ρ) vs temperature (T) measurement at several pressure values. The temperature variation of resistivity from room temperature to 22 K at several pressure values is shown in Fig. 6. In the pressure range, ambient to about 5.1 GPa, the resistivity is found to decrease with a decrease in temperature indicating a metallic characteristic and then show an upturn at low temperatures. At ambient pressure, $\rho(T)$ curve takes an upturn at about 58 K and increases with the decrease in temperature showing a broad minimum. We find that the initial slope of the decrease in $\rho(T)$ vs T decreases with pressure and also the low temperature minimum becomes flatter. Interestingly, at about 7.3 GPa, we find a rise in $\rho(T)$ values with the decrease in T, and also the ρ value obtained at the lowest temperature shows a large increase. Another important aspect is that the resistivity also decreases with pressure at room temperature up to about 5 GPa, followed by a saturation, as shown in the inset of Fig. 6. The change in temperature behavior of resistivity above 5 GPa indicates a change in the electronic property of the sample, which is evident from our structural investigations in terms of a minimum in c/a ratio and a minimum in the FWHM of the A_{1g} Raman mode.

In an effort to understand the anomalous behavior of resistivity of the sample with temperature and pressure, it is important to understand the ambient pressure data. We shall initially try to understand the metallic characteristic of the sample, though several previous theoretical studies have predicted ZrSe$_2$ to be an indirect band gap semiconductor having a moderate band gap in the range of 0.9–1.2 eV similar to silicon [36,41]. A recent study on a sister TMD, ZrTe$_2$ has shown it to be metallic and EDAX measurements have shown an excess of about 10 at.% Zr in the host [23]. Intercalation of a trace amount of Re (about 1.3% wt.) inside the layers of pure ZrSe$_2$ has resulted in metallic behavior of the sample [20]. Another theoretical study has shown that structural defects in the pristine ZrSe$_2$ crystal can change its magnetic and electronic properties including metallic behavior [42]. Therefore, we believe that the presence of additional 3 at.% of Zr may result in the metallic characteristic shown by the present sample at ambient and high pressures. Let us first look into the temperature dependence of resistivity at ambient pressure. In our experiments, it is found that the resistivity varies linearly with temperature above 200 K. Variation of resistivity linearly with the temperature is a signature of electron-phonon scattering because the total number of phonons for scattering at high temperature is directly proportional to T [43]. This signifies phonon scattering is the dominant scattering mechanism at high temperatures. Above 195 K the $\rho(T)$ vs T data is fitted to the expression

$$\rho(T) = C + DT, \tag{2}$$

where C and D are the fitting parameters. Below 195 K up to 70 K, resistivity does not vary linearly with temperature. In
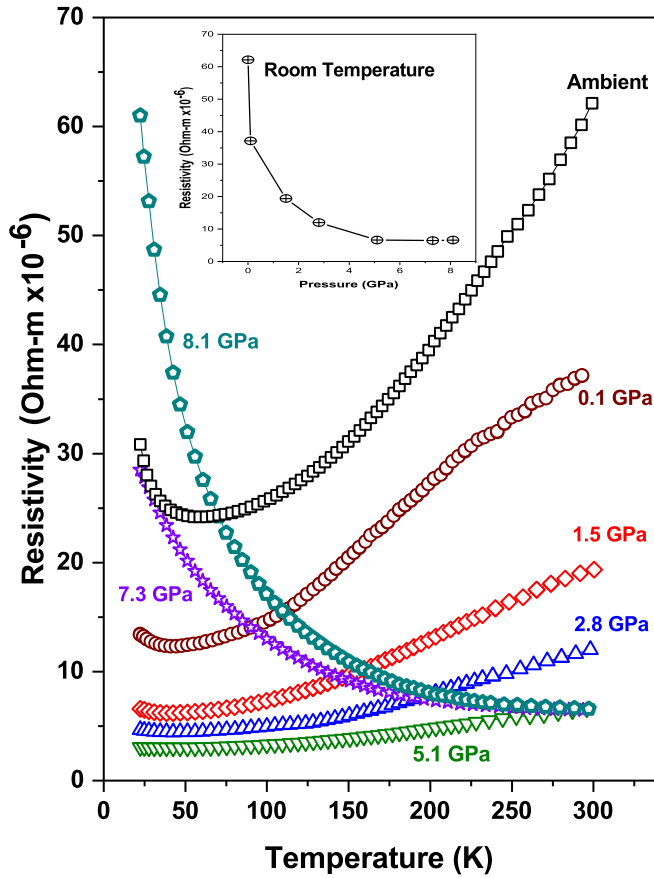
FIG. 6. Temperature variation of resistivity at different pressure points. Pressure variation of room temperature resistivity is shown in inset.

this region ρ vs T data is best fitted to the expression

$$\rho(T) = \rho_0 + AT^2 + BT^5, \qquad (3)$$

where ρ_0, A, and B are the fitting parameters. At low temperature, the electron-phonon scattering has a T^5 dependence [43]. The T^2 dependence of resistivity comes from the electron-electron scattering [44]. Below 58 K, the ρ is found to increase with lowering in T, indicating a possibility of metal to insulator transition. Therefore, we have tried to fit our data to $\ln\rho$ vs $1/T$, which did not yield a linear nature (Supplemental Fig. S13 [26]) and hence one can discard a metal to insulator transition in the sample at these low temperatures.

In strongly correlated layered systems, the upturn in $\rho(T)$ behavior can be attributed to the electron-electron interaction, weak localization, or Kondo effect [45–48]. In the absence of high pressure resistivity measurements under a magnetic field, we shall try to use the phenomenological models and discuss the possible phenomena for the upturn in resistivity at low temperatures. The application of pressure reduces the resistivity of the sample as well as the upturn becomes flatter until about 5.1 GPa. Therefore, due to the increase in conductivity with pressure, one can ignore the effect of weak localization. Similarly, the electron-electron interaction gives a $T^{-\frac{1}{2}}$ dependence in $\rho(T)$ [45,47]. However, as shown in Supplemental Fig. S14 [26], we do not see any linear dependence of $\ln\rho(T)$ with respect to $\ln T$.
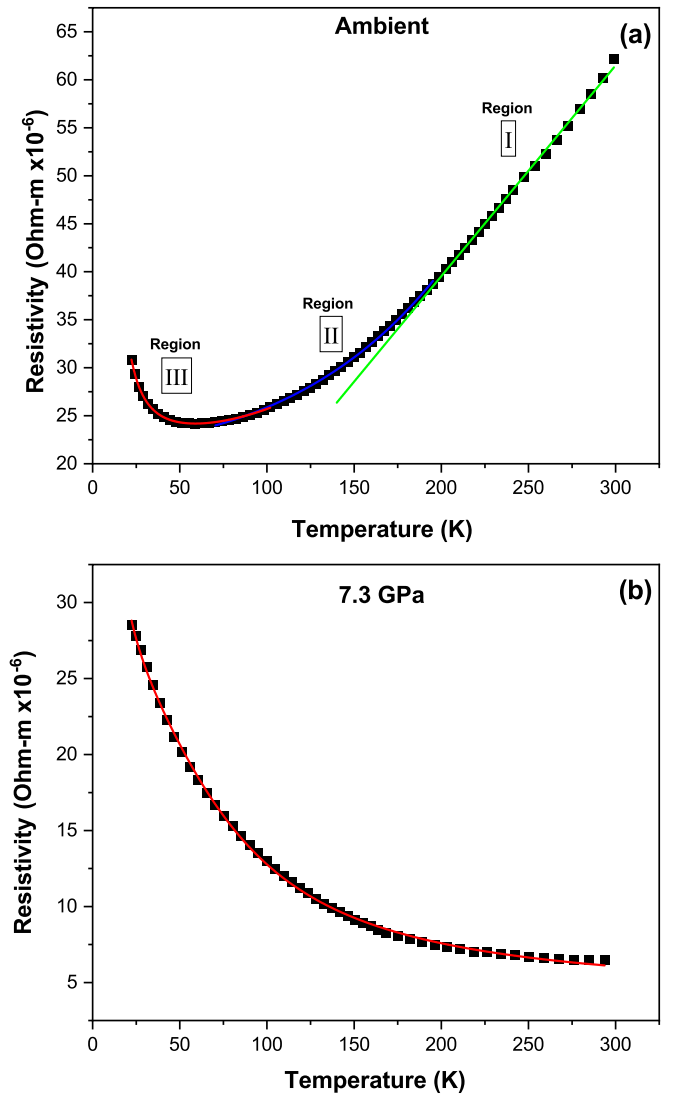
FIG. 7. (a) Temperature variation of resistivity at ambient pressure. Region I is fitted to Eq. (2), region II is fitted to Eq. (3), and region III is fitted to Eq. (4). Solid lines through the data points show respective fits. (b) Temperature variation of resistivity at 7.3 GPa. The solid line through the data points shows the fit to the combined Eq. (4) and Eq. (5), keeping the values of A and B zero and E_g constant.

In the absence of high pressure low temperature resistivity measurements under a magnetic field we have treated our low temperature ρ vs T data using the phenomenological Kondo model. Following the literature, we have fitted our resistivity data at low temperatures to the equation [23,49]

$$\rho(T) = \rho_C + AT^2 + BT^5$$
$$+ \rho_K \left[1 - \ln\left(\frac{T}{T_K}\right) \left\{ \ln^2\left(\frac{T}{T_K}\right) + S(S+1)\pi^2 \right\}^{-\frac{1}{2}} \right], \qquad (4)$$

where the fitting parameters ρ_C, ρ_K, T_K, and S represent the residual resistivity, temperature-independent resistivity, Kondo temperature, and the average spin of magnetic

TABLE II. Fitting parameters obtained from resistivity studies at different pressure points.

Pressure (GPa)	$\rho_c \times 10^{-6}$ (Ω m)	$A \times 10^{-11}$ (Ω m K^{-2})	$B \times 10^{-18}$ (Ω m K^{-5})	$\rho_k \times 10^{-7}$ (Ω m)	T_k (K)	S	$D \times 10^{-8}$ (Ω m K^{-1})
0	20.79(6)	35.4(8)	11.6(9)	349(6)	12.3(8)	0.032(4)	21.9(1)
0.1	10.89(4)	36(1)	13.8(2)	23(2)	22(1)	0.048(5)	10.6(1)
1.5	5.677(4)	15.1(1)	6.6(2)	7.2(2)	24.5(4)	0.034(1)	6.74(3)
2.8	4.261(5)	5.81(4)	5.2(7)	3.0(2)	25.0(8)	0.030(2)	4.15(1)
5.1	2.891(7)	3.57(5)	1.8(1)	0.8(1)	31(2)	0.03(1)	1.90(2)

Pressure (GPa)	$\rho(0)$ (Ω m $\times 10^{-7}$)	E_g (eV)	ρ_k (Ω m $\times 10^{-5}$)	T_k (K)	S
7.3	19(6)	0.0015(1)	1.57(5)	60(1)	0.16(1)
8.1	20(1)	0.0044(3)	3.21(7)	51(1)	0.13(1)

impurities, respectively, and the data fits well with the model. Since Eq. (4) has several parameters, we first extracted the values of A and B by fitting $\rho(T)$ in the temperature range 195 K to 70 K (region II) to Eq. (3). Then $\rho(T)$ data in the temperature region 101 K to 22 K (region III) is fitted to Eq. (4) by keeping the values of parameters A and B fixed to the values obtained from the earlier fit. All the parameter values are given in Table II. We shall discuss the pressure behavior of the parameters S and T_K later in the Discussion section.

At and above 7.3 GPa the nature of temperature variation of resistivity changes dramatically. It starts to increase with the lowering of temperature showing a semiconducting type behavior [Fig. 7(b)] at 7.3 GPa. The observation of a pressure induced metal to semiconductor transition is rarely reported in the literature. In a semiconductor, the resistivity varies with temperature as

$$\rho(T) = \rho(0)\exp^{\left(\frac{E_g}{2K_B T}\right)}, \qquad (5)$$

where K_B is the Boltzmann constant and E_g is the band gap. But the data at 7.3 and 8.1 GPa in the whole temperature range could not be fitted using only the exponential term as the $\ln\rho(T)$ vs $1/T$ does not show a linear behavior (Supplemental Fig. S16 [26]). We have also tried to fit the 7.3 GPa data to Eq. (4), which also did not produce a good fit (Supplemental Fig. S17 [26]). We have tried to fit the data to the magnetic part of Eq. (4) only, keeping the coefficients of T^2 and T^5 terms to zero, but that also does not fit Fig. S18 well [26]. We would like to point out here that our experimental setup limits the low temperature value to about 22 K at the sample. Therefore, we carried out a linear fit in the range of 22–35 K for the data at 7.3 GPa and 22–50 K for the data at 8.1 GPa for $\ln\rho(T)$ vs $1/T$. This produced a E_g value of about 1.5(1) meV and 4.4(3) meV at 7.3 GPa and 8.1 GPa, respectively. Such small values of band gap indicate that, at these high pressures, the $Zr_{1.03}Se_2$ is an almost zero gap semiconductor. Matsuoka and Shimizu reported a similar semimetal to zero gap semiconductor transition in Li at extreme high pressures, where the band gap was estimated to be about 0.83 meV at about 78 GPa [50]. But in the present case, the value of E_g increased with pressure, where it was found to decrease with pressure for Li. When we fitted the combined Eq. (4)

and Eq. (5) to our data by keeping the values of A and B zero and considering the value of E_g obtained from low temperature data, with $\rho(0)$, S, and T_K being the three fitting parameters, it produced a good fit [Fig. 7(b)]. Therefore, it seems that the mixed phase opens up a very small band gap in the sample.

In a theoretical study, Zhai *et al.* [6] have shown the monoclinic phase of ZrS_2 to be a narrow band gap semiconductor with the band gap of 0.738 eV. It has been observed in several hcp metals and alloys that the c/a ratio affects the electronic orbital hybridization and can result in a change in the electronic band structure near the Fermi surface. The observed minimum in the c/a ratio in the present case may be driving a change in the electronic band structure and may result in the opening of a small gap near the Fermi surface [51–53]. In fact, a recent study has shown that tuning the strain on a monolayer 1T' WTe_2 has led to a semimetal to topological insulator transition [54]. Our XRD studies show that, at high pressures beyond 5.9 GPa, both the 1T and the monoclinic phases show anisotropic compression behavior along different axial directions, resulting in differential strain in the unit cell. Therefore, it may also cause a change in the Fermi surface topology resulting in the opening of a very small band gap. Other systematic behavior observed is a decrease in the ambient temperature ρ until about the phase transition pressure. The 1T phase shows large compressibility resulting in a large decrease in volume, which includes about 6.4% decrease in the average Zr-Se bond length and a reduction in the unit cell strain. This structural change possibly results in further enhancement of overlap of electronic orbitals leading to a decrease in the electron scattering events and hence an increase in electronic conduction to about 5.1 GPa.

In a recent work on a sister layered TMD, $ZrTe_2$, an upturn in the resistivity values at low temperatures is reported and is explained due to the Kondo effect arising from additional 10 at.% Zr atom present in the material [23]. A similar situation may arise due to the presence of additional 3 at.% Zr in the present case. The electron configuration of the Zr atom is $[Kr]5s^2 4d^2$. The presence of two unpaired electrons at the $4d$ orbital gives rise to a spin magnetic moment $S = 1$. Therefore, the presence of excess Zr atoms in our sample can act as magnetic impurity embedded in the material. The magnetic

impurity can give rise to the resistivity upturn due to the Kondo effect. From the fit of the temperature dependent resistivity data at ambient pressure, the average impurity spin per Zr atom is obtained to be $S = 0.0326$. Then the spin for excess Zr can be calculated as $(0.0326 \times 1.033) \div 0.033 = 1.02 \approx 1$. This is consistent with the expected total spin value of the Zr atom. The ρ vs T data at high pressure up to 5.1 GPa are similarly analyzed in three different temperature regions (Supplemental Fig. S15 [26]). The depth of the Kondo anomaly reduces with the application of pressure. The S values seem to remain almost constant until 5.1 GPa (Table II). However, T_K is found to increase with pressure. In the mixed phase, the values of T_K and S are found to be larger in comparison to the values obtained from the pure 1T phase. Investigations on the pressure effect of the Kondo temperature in several systems have shown an increase in Kondo temperature with pressure [55–57]. In Cu:Fe and Au:Fe Kondo alloys the pressure induced doubling of Kondo temperature has been explained using a simple model of pressure-induced broadening of the bound state of the impurity Fe atom and hence increasing the intermixing of the bands [55–57]. In another study on the Ce and Yb based heavy fermion compounds, it has been shown that the increase in the hybridization of f electron states and conduction electron states results in an increase of the Kondo temperature with pressure [58]. Therefore, in view of the above facts we believe that the increase in intermixing of the d-electron states of the Zr atom resulting in broadening of the bound state of the impurity atom due to a large decrease in volume and anisotropic compression of the lattice leads to a large change in the J_{exchange} value in the lattice. In fact, the XRD studies show that there is an increase in the effective coordination number of Zr-Se6 octahedra from 1 in the 1T structure to a value of about 1.17 in the monoclinic structure at about 7 GPa, indicating modification of the J_{exchange} value leading to an increase in the Kondo temperature and the average spin. But additional theoretical and high pressure experimental studies under magnetic field are necessary to get to a definite conclusion about the observed interesting behavior in the present work. The present work shows a close relationship between the effect of impurity and strain on the electronic behavior of transition metal dichalcogenides.

IV. CONCLUSIONS

1T $Zr_{1.03}Se_2$ undergoes a pressure induced gradual structural phase transition, which starts around 5.9 GPa and completes around 14.8 GPa. Though the high pressure phase could be indexed to both orthorhombic and monoclinic crystal structures, the Rietveld analysis produced a better fit for the monoclinic structure. High pressure Raman measurements show the appearance of several new Raman modes above 5.9 GPa, similar to the pressure where the new structural phase starts to grow along with the parent phase. The appearance of new Raman modes is attributed to the change in symmetry in the sample due to the transition to a lower symmetry monoclinic phase. A minimum in FWHM of the A_{1g} Raman mode at about 5 GPa shows an increase in the phonon lifetime and indicates the presence of an electronic phase transition. The electronic phase transition is confirmed by the low temperature and high pressure resistivity measurements of the sample. The low temperature resistivity data at all pressure values show an upturn which is possibly due to the Kondo anomaly in the sample due to the presence of additional Zr, which acts as the magnetic impurity. With the application of pressure, the depth of the Kondo anomaly reduces. The temperature dependent resistivity data show that in the mixed phase a small band gap opens in the sample resulting in a pressure induced metal to semiconductor transition.

[1] S. U. Rehman and Z. Ding, Phys. Chem. Chem. Phys. **20**, 16604 (2018).

[2] Q. Song, H. Wang, X. Pan, X. Xu, Y. Wang, Y. Li, F. Song, X. Wan, Y. Ye, and L. Dai, Sci. Rep. **7**, 1 (2017).

[3] D. H. Keum, S. Cho, J. H. Kim, D.-H. Choe, H.-J. Sung, M. Kan, H. Kang, J.-Y. Hwang, S. W. Kim, H. Yang, K. J. Chang, and Y. H. Lee, Nat. Phys. **11**, 482 (2015).

[4] Y. Kvashnin, D. VanGennep, M. Mito, S. A. Medvedev, R. Thiyagarajan, O. Karis, A. N. Vasiliev, O. Eriksson, and M. Abdel-Hafiez, Phys. Rev. Lett. **125**, 186401 (2020).

[5] S. Sahoo, U. Dutta, L. Harnagea, A. K. Sood, and S. Karmakar, Phys. Rev. B **101**, 014514 (2020).

[6] H. Zhai, Z. Qin, D. Sun, J. Wang, C. Liu, N. Min, and Q. Li, Phys. Chem. Chem. Phys. **20**, 23656 (2018).

[7] U. Dutta, P. S. Malavi, S. Sahoo, B. Joseph, and S. Karmakar, Phys. Rev. B **97**, 060503(R) (2018).

[8] X.-M. Zhao, H.-Y. Liu, A. F. Goncharov, Z.-W. Zhao, V. V. Struzhkin, H.-K. Mao, A. G. Gavriliuk, and X.-J. Chen, Phys. Rev. B **99**, 024111 (2019).

[9] L. F. Mattheiss, Phys. Rev. B **8**, 3719 (1973).

[10] J. A. Wilson and A. D. Yoffe, Adv. Phys. **18**, 193 (1969).

[11] F. Wypych and R. Schöllhorn, J. Chem. Soc., Chem. Commun. 1386 (1992).

[12] R. Bissessur, M. G. Kanatzidis, J. L. Schindler, and C. R. Kannewurf, J. Chem. Soc., Chem. Commun. 1582 (1993).

[13] B. Ghosh, P. Saha, B. Mukherjee, D. Samanta, G. Shukla, and G. D. Mukherjee, Electron. Struct. **3**, 045002 (2021).

[14] P. Saha, B. Ghosh, R. Jana, and G. D. Mukherjee, J. Appl. Phys. **123**, 204306 (2018).

[15] P. Saha, B. Ghosh, A. Mazumder, and G. D. Mukherjee, Mater. Res. Express **7**, 025902 (2020).

[16] P. Saha, B. Ghosh, A. Mazumder, K. Glazyrin, and G. D. Mukherjee, J. Appl. Phys. **128**, 085904 (2020).

[17] A. Kumar, H. He, R. Pandey, P. Ahluwalia, and K. Tankeshwar, Phys. Chem. Chem. Phys. **17**, 19215 (2015).

[18] N. Bandaru, R. S. Kumar, D. Sneed, O. Tschauner, J. Baker, D. Antonio, S.-N. Luo, T. Hartmann, Y. Zhao, and R. Venkat, J. Phys. Chem. C **118**, 3230 (2014).

[19] G. Q. Huang, Z. W. Xing, and D. Y. Xing, Phys. Rev. B **93**, 104511 (2016).

[20] Z. ur Rehman, S. Wang, M. A. Lawan, S. Zareen, O. A. Moses, W. Zhu, X. Wu, Z. Sun, and L. Song, Appl. Phys. Lett. **115**, 213102 (2019).

[21] A. Shkvarin, A. Merentsov, Y. M. Yarmoshenko, M. Postnikov, E. Shkvarina, A. Titov, I. Pis, S. Nappini, F. Bondino, and A. Titov, J. Phys. Chem. C **123**, 410 (2019).

[22] S. Tang, C. Zhang, C. Jia, H. Ryu, C. Hwang, M. Hashimoto, D. Lu, Z. Liu, T. P. Devereaux, Z.-X. Shen, and S.-K. Mo, APL Mater. **6**, 026601 (2018).

[23] Y. Wang, C. Xie, J. Li, Z. Du, L. Cao, Y. Han, L. Zu, H. Zhang, H. Zhu, X. Zhang, Y. Xiong, and W. Zhao, Phys. Rev. B **103**, 174418 (2021).

[24] S. Mañas-Valero, V. García-López, A. Cantarero, and M. Galbiati, Appl. Sci. **6**, 264 (2016).

[25] M. Salavati, Front. Struct. Civ. Eng. **13**, 486 (2019).

[26] See Supplemental Material at http://link.aps.org/supplemental/10.1103/PhysRevB.106.104102 for additional figures and tables in support of the analysis carried out in the manuscript.

[27] H. Mao, J.-A. Xu, and P. Bell, J. Geophys. Res. **91**, 4673 (1986).

[28] C. Prescher and V. B. Prakapenka, High Press. Res. **35**, 223 (2015).

[29] A. Dewaele, M. Torrent, P. Loubeyre, and M. Mezouar, Phys. Rev. B **78**, 104102 (2008).

[30] R. Shirley, *The CRYSFIRE System for Automatic Powder Indexing: User's Manual* (The Lattice Press, Guildford, UK, 1999).

[31] B. H. Toby, J. Appl. Cryst. **34**, 210 (2001).

[32] D. Vaughan, Br. J. Appl. Phys. **12**, 414 (1961).

[33] L. J. van der Pauw, Philips Res. Repts. **13**, 1 (1958).

[34] C. Gao, Y. Han, Y. Ma, A. White, H. Liu, J. Luo, M. Li, C. He, A. Hao, X. Huang, Y. Pan, and G. Zou, Rev. Sci. Instrum. **76**, 083912 (2005).

[35] J. Laugier and B. Bochu, LMGP-Suite of Programs for the Interpretation of X-ray Experiments, ENSP/Laboratoire des Matériaux et du Génie Physique, F. BP 46, 38042 Saint Martin d'Hères, 2004.

[36] E. Martino, D. Santos-Cottin, F. L. Mardelé, K. Semeniuk, M. Pizzochero, K. Černevičs, B. Baptiste, L. Delbes, S. Klotz, F. Capitani, H. Berger, O. V. Yazyev, and A. Akrap, ACS Mater. Lett. **2**, 1115 (2020).

[37] F. Birch, Phys. Rev. **71**, 809 (1947).

[38] J. F. Ahmad and I. Y. Alkammash, J. Assoc. Arab Univ. Basic Appl. Sci. **12**, 17 (2012).

[39] K. Nikonov, N. Ehlen, B. Senkovskiy, N. Saigal, A. Fedorov, A. Nefedov, C. Wöll, G. Di Santo, L. Petaccia, and A. Grüneis, Dalton Trans. **47**, 2986 (2018).

[40] S. Klotz, J. Chervin, P. Munsch, and G. L. Marchand, J. Phys. D: Appl. Phys. **42**, 075413 (2009).

[41] A. Ghafari, M. Moustafa, G. D. Santo, L. Petaccia, and C. Janowitz, Appl. Phys. Lett. **112**, 182105 (2018).

[42] Y. Gao, X. Zhao, H. Wang, T. Wang, and S. Wei, Comput. Mater. Sci. **146**, 36 (2018).

[43] N. W. Ashcroft and N. D. Mermin, in *Solid State Physics*, edited by D. G. Crane (Saunders College, Philadelphia, 1976).

[44] A. Thompson, Phys. Rev. Lett. **35**, 1786 (1975).

[45] Y. Xu, J. Zhang, G. Cao, C. Jing, and S. Cao, Phys. Rev. B **73**, 224410 (2006).

[46] M. Ziese, Phys. Rev. B **68**, 132411 (2003).

[47] T. Okuda, T. Kimura, and Y. Tokura, Phys. Rev. B **60**, 3370 (1999).

[48] P. A. Lee and T. Ramakrishnan, Rev. Mod. Phys. **57**, 287 (1985).

[49] D. R. Hamann, Phys. Rev. **158**, 570 (1967).

[50] T. Matsuoka and K. Shimizu, Nature (London) **458**, 186 (2009).

[51] U. Häussermann and S. I. Simak, Phys. Rev. B **64**, 245114 (2001).

[52] Y. Fujinaga, S. Hashimoto, K. Fukamichi, and T. Kikegawa, High Press. Res. **11**, 271 (1993).

[53] S. Sinha, S. S. Nene, M. Frank, K. Liu, P. Agrawal, and R. S. Mishra, Sci. Rep. **9**, 13185 (2019).

[54] C. Zhao, M. Hu, J. Qin, B. Xia, C. Liu, S. Wang, D. D. Guan, Y. Li, H. Zheng, J. Liu, and J. Jia, Phys. Rev. Lett. **125**, 046801 (2020).

[55] J. S. Schilling and W. Holzapfel, Phys. Rev. B **8**, 1216 (1973).

[56] M. Maple and J. Wittig, Solid State Commun. **9**, 1611 (1971).

[57] K. Kim and M. Maple, Phys. Rev. B **2**, 4696 (1970).

[58] A. Goltsev and M. Abd-Elmeguid, J. Phys.: Condens. Matter **17**, S813 (2005).